

Experimental investigation of lean premixed pre-vaporized liquid-fuel combustion in porous media burners at elevated pressures up to 20 bar

Sadaf Sobhani^{a,*}, Justin Legg^b, David F. Bartz^b, Jun J. Kojima^c, Clarence T. Chang^d, John D. Sullivan^b, Jeffrey P. Moder^d, Matthias Ihme^a

^a Department of Mechanical Engineering, Stanford University, Stanford, CA 94305, USA

^b Alzeta Corporation, Santa Clara, CA 95054, USA

^c Ohio Aerospace Institute, Cleveland, OH 44142, USA

^d NASA John H. Glenn Research Center, Cleveland, OH 44135, USA

ARTICLE INFO

Article history:

Received 29 June 2019

Revised 21 October 2019

Accepted 22 October 2019

Keywords:

Porous media combustion

Ceramic foams

Gas-turbines

Liquid fuel

High pressure combustion

ABSTRACT

Combustion in porous media has been identified as a promising technology for achieving higher burning rates, extending flammability limits, and reducing emissions. To assess the viability of this technology for application to aviation gas-turbine engines, the performance of a Porous Media Burner (PMB) operated with pre-vaporized liquid fuel at high pressures is experimentally examined. The PMB was operated at fuel-lean equivalence ratios between 0.4 and 0.55 at pressures up to 20 bar with fully pre-vaporized and preheated n-heptane as well as gaseous methane at 8 bar for performance comparison. Combustion stability maps are reported along with temperature profiles, pressure drops, and emissions of CO and NO_x at stable operating conditions. Results from these experiments show excellent performance of PMBs at high-pressure conditions. Additionally, numerical simulations using the volume-averaged, one-dimensional reacting flow-equations complement the experimental measurements to provide further insight into the effects of the pressure and fuel mixture on the flame structure. Lastly, high-resolution es X-ray Computed Tomography (XCT) is used to examine the structural integrity of the porous matrix during the high-pressure combustion operation, showing evidence of micro-fissures and an increase in the surface roughness due to SiC-oxidation. Large-scale defects were not observed after four days of cyclic high-pressure testing over a wide range of pressures, heating rates, and equivalence ratios.

© 2019 The Combustion Institute. Published by Elsevier Inc. All rights reserved.

1. Introduction

Increasingly stringent emission regulations for aviation gas-turbine engines motivate the need for novel combustion system designs that enable reliable operation near the fuel-lean flammability limit. The implementation of advanced combustion concepts, such as porous media combustion, offers the potential to reduce emissions, as well as achieve enhanced flame stabilization and improved fuel efficiency. Porous media combustion entails combustion within the cavities of an inert porous medium, in contrast to conventional burners that utilize a free flame [1,2].

Porous Media Burners (PMBs) facilitate internal heat recirculation from the combustion products to the reactants upstream via conduction and radiation in the solid porous matrix. Typically,

porous materials used in PMBs consist of ceramic or other heat-conducting foams that have large surface-to-volume ratios, thereby enabling direct heat exchange between the solid and gas phases, and high porosities for minimizing the pressure drop. Due to the internal heat recirculation, PMBs exhibit higher reactant temperatures, which lead to faster flame speeds and an extension of the flammability limit to leaner conditions. Stable burner operation at such fuel-lean conditions enables reduced NO_x and CO production.

Flame stabilization in PMBs can be predicted from the analysis of the solid matrix conductivity, optical depth and the local Stanton number, which is the ratio of the interphase heat exchange to the convective transport [3]. The optical depth is increased with decreasing pore diameter, thus if the porous media is sufficiently opaque, radiation becomes ineffective at recirculating heat. As PMBs also operate on the principle of effective interphase heat exchange, the Stanton number is an important parameter for predicting trends in burner performance. The mass flux is inversely proportional to the Stanton number, thus, increasing the operating

* Corresponding author.

E-mail address: ssobhani@stanford.edu (S. Sobhani).

flow rates of the burner reduces the preheating of the incoming reactants from the solid, eventually leading to flame blow-off. Instead of relying on this dynamic heat balance, PMBs can be designed to anchor the flame at one location. Most existing PMBs utilize this “interface-stabilized” burner design, which operates on the principle that the upstream region serves as a flame arrestor and the downstream region as the combustion zone [4]. The modified Péclet number was introduced to characterize the local ratio of heat release by combustion to heat removal in a PMB [5]. The flame is stabilized at the interface between the two regions that are above and below the critical Péclet number for flame quenching.

Previous experimental and computational studies of lean premixed combustion of gaseous fuel at atmospheric pressure in PMBs have illustrated several performance advantages compared to conventional burners [3,6–11]. Investigations of lean premixed porous media combustion at elevated pressure are less common and were mainly performed using gaseous fuels. Bedoya et al. [12] utilized a conical PMB with natural gas as the fuel source, and reported enhanced burning velocities for pressures up to 14 bar. Noordally et al. [13] studied combustion of methane-air mixtures at lean conditions up to 11 bar, and found that the propensity of flashback increases with increasing pressure. Bakry et al. [14] also utilized a conical PMB operated with methane at lean conditions up to 9 bar.

The combustion of liquid fuels in PMBs has been examined, although these investigations were largely limited to atmospheric pressure conditions. These studies demonstrated similar performance advantages as those of gaseous fuel burners, such as higher burning rates, extended lean flammability limits, and reduced emissions. Liquid-fuel combustion in a PMB was first experimentally investigated by Kaplan and Hall [15]. Liquid n-heptane was delivered to a nozzle and sprayed onto a porous foam upstream of the main PMB. Radiant pre-heating from the main PMB, as well as flow through the upstream porous foam, enhanced the fuel-droplet evaporation and mixing. Stable combustion was observed for equivalence ratios between $\phi = 0.57$ and 0.67. Emissions of CO were reported ranging from 3–7 ppm and NO_x from 15–20 ppm. No accumulation of soot or pore plugging was observed. Tseng and Howell [16] experimentally and computationally investigated the operation of liquid n-heptane in a PMB, and found stable operation for equivalence ratios as lean as $\phi = 0.3$. Emissions were reported to be very low, with $\text{CO} < 10$ ppm and $\text{NO}_x < 20$ ppm. Combustion of kerosene in a PMB was investigated by Vijaykant and Agrawal [17], using both an air-assist injector and a swirl-air injector.

In all the aforementioned studies of liquid fuel PMBs, the distance between the injector and the porous media was reported as a critical factor to maintain stable combustion. To eliminate the need of using a fuel atomizer, both Takami et al. [18] and Jugjai et al. [19] directly supplied kerosene to the top surface of the PMB, via a steel wire net to achieve a uniform droplet distribution. Stable combustion was achieved over equivalence ratios ranging from 0.1 to 0.9.

Due to the high volumetric heat release of PMBs, incineration of liquid hazardous waste was proposed as a potential application of liquid fuel combustion in porous media [15]. PMBs at elevated pressures also have potential applications in clean gas-turbine operation [13]. In a recent study, the effect of porous media combustion on the thermodynamic cycle performance of gas-turbine engines was evaluated and shown to enable an appreciable increase in thermodynamic efficiency and reduction of emissions by extending the nominal lean flammability limit, thereby allowing for engine operation at higher pressure ratios and lower dilution ratios [20].

As outlined above, most of the existing literature on examining the operation of porous media combustion at elevated pressures

has been limited to gaseous fuels, while investigations of liquid fuels only consider atmospheric pressure conditions. By addressing this gap, the objective of this study is to experimentally examine the performance of an “interface-stabilized” PMB that is operated with pre-vaporized liquid fuel at high-pressure conditions. The design of the test rig and operating conditions were motivated by the expected pressure and temperature at the combustor inlet of a high-bypass ratio turbo-fan engine at cruise and take-off conditions to examine the viability of porous media combustion for application to aviation gas-turbine engines. To focus on the combustion process and eliminate complexities associated with the liquid-fuel atomization, the fuel is pre-vaporized upstream of the burner. The experiment is instrumented with thermocouples, pressure sensors, and an exhaust-emissions probe to measure temperature profiles, pressure loss, and combustion products of CO and NO_x . These measurements are complemented by numerical simulations using the volume-averaged, one-dimensional reacting flow-equations to provide insight about the effect of the pressure and fuel mixture on the flame structure. Results from these computational investigations are presented in the next section. The experimental setup and results from the high-pressure measurements are discussed in Section 3. To provide insights into the structural integrity of commonly used ceramic foams in PMBs, pre- and post-combustion analysis of the porous structure using high-resolution X-ray Computed Tomography (XCT) is presented and discussed in Section 4. Finally, conclusions are presented in Section 5.

2. Computational analysis

To provide a general understanding of the high-pressure effects on the flame structure, numerical simulations of the PMB are performed at conditions that are experimentally studied. The equations governing the combustion in porous media are derived by volume-averaging of the transport equations for a chemically reacting gaseous system [21]. Numerical simulations were performed using the CANTERA 1D reacting flow solver, which was adapted to account for the coupling between the gas and solid phases in the PMB calculations. The reaction chemistry was modeled using a 68-species skeletal mechanism for n-heptane [22] and the DRM-19 mechanism, derived from the GRI-Mech 1.2, for methane [23]. More details on the governing equations, model assumptions, and the computational method can be found in [3,11].

In the simulations, the inlet temperature was 470 K and the operating pressure varied from 2 to 20 bar to match the experimental conditions. Both of the chemical mechanisms implemented have been previously validated at elevated pressures for the fuel-lean conditions tested (i.e. $\phi = 0.57$). The upstream section is modeled as a 5.08 cm porous material with 82% porosity, 0.25 mm pore size, and 0.30 W/(m K) thermal conductivity. The downstream section is 2.54 cm in length, 89% porosity, 1.1 mm pore size, and 1.5 W/(m K) thermal conductivity. The material, length, pore size, and porosity distribution of the burner in the simulation were chosen to match those of the experiment, as described in Section 3.1.

Figure 1 shows comparisons of flame profiles between free flames and PMBs for a range of pressure conditions and mass flux rates. In the governing equations, the gas and solid temperatures are coupled by the convective heat transfer, $h_v(T_g - T_s)$. Therefore, in addition to the gas and solid temperature profiles, the heat transfer coefficient, h_v , is presented to give insights into the effects of pressure on the flame. First, Fig. 1(a) illustrates the temperature profiles of n-heptane free flames at 2, 8, and 20 bar, as well as methane at 8 bar, all at $\phi = 0.57$. The results indicate a ~ 50 K difference in flame temperature in the methane 8 bar flame, as compared to n-heptane, and small differences with increasing pressure near the reaction zone. However, the results show appreciable differences in the flame structure for PMB-flames. First, as shown in

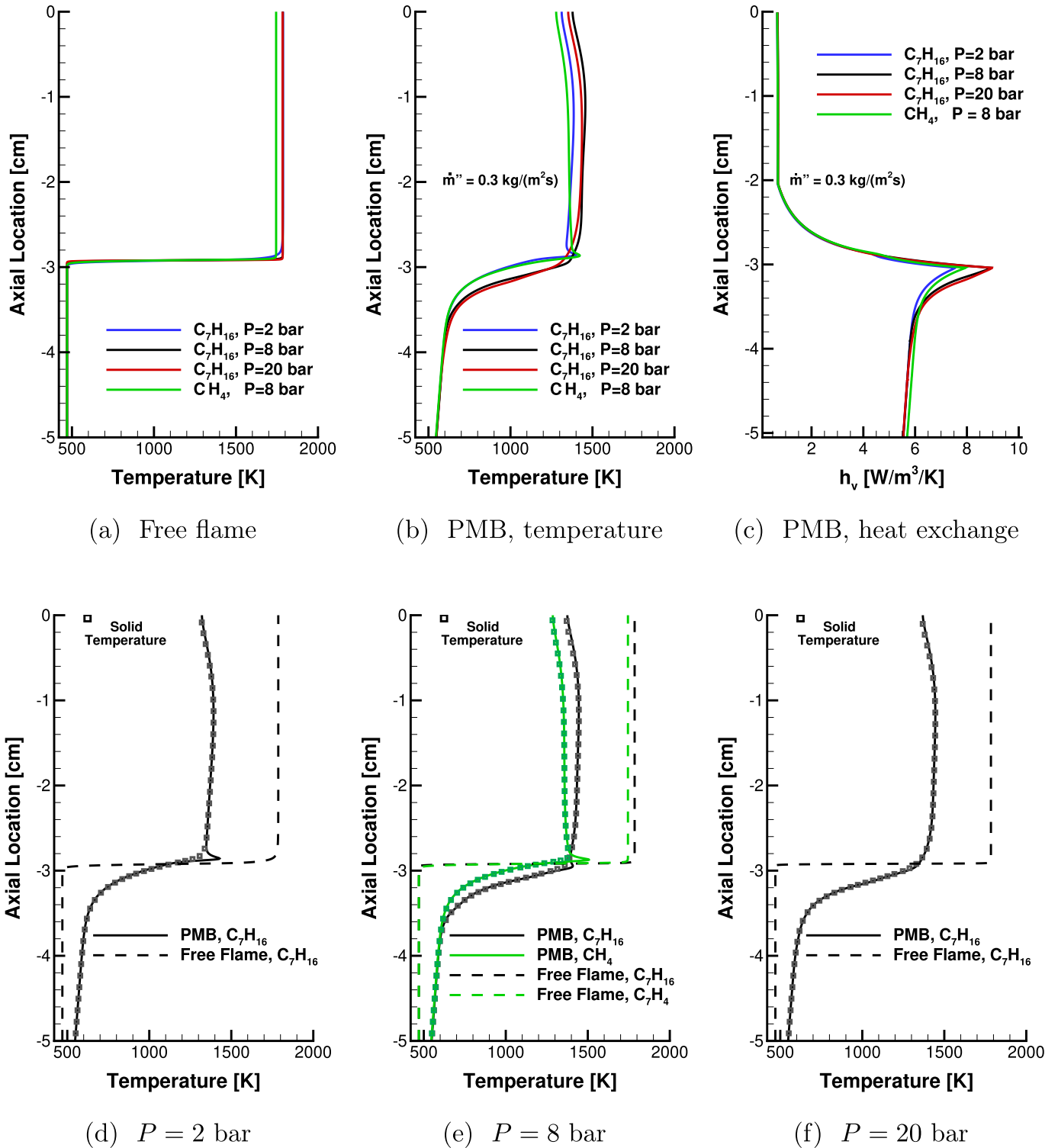
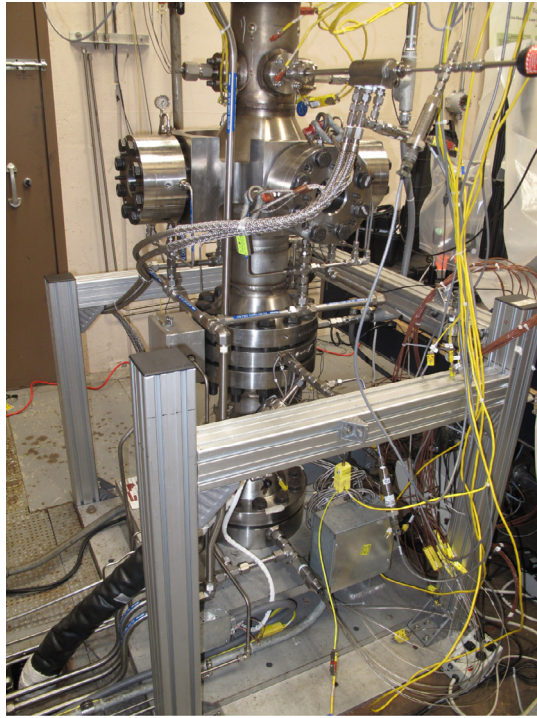


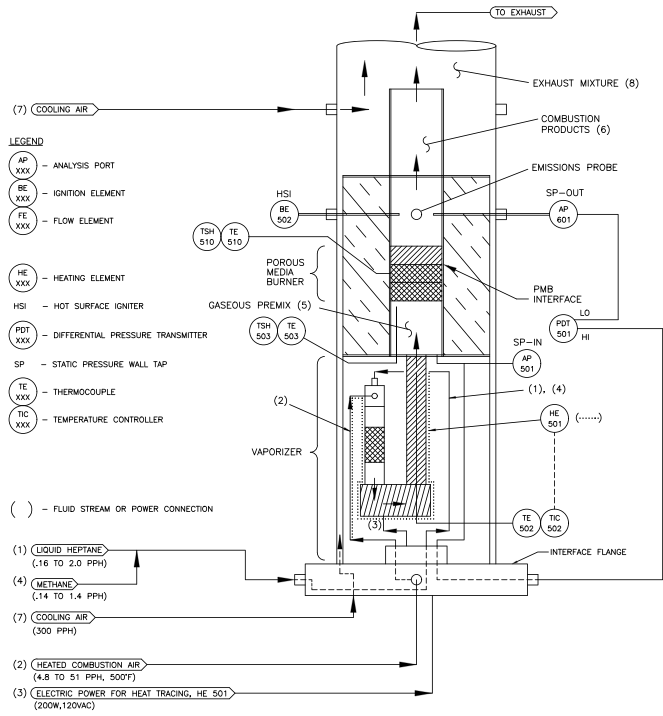
Fig. 1. Computational profiles at $\phi = 0.57$ of (a), (b) gas temperature for free flames and PMB, and (c) heat transfer coefficient in PMB. In (d)–(f), the mass flux rate in the PMB simulation corresponds to that of the n-heptane free flame at 2, 8, and 20 bar, equal to 0.4, 0.87, and 1.34 $\text{kg}/(\text{m}^2\text{s})$, respectively and 0.47 $\text{kg}/(\text{m}^2\text{s})$ for methane at 8 bar. Symbols indicate the predicted solid-phase temperature. (For interpretation of the references to color in this figure legend, the reader is referred to the web version of this article.)

Fig. 1(b), at a fixed mass flux rate of 0.3 $\text{kg}/(\text{m}^2\text{s})$ and increasing pressure, the exit temperature for the n-heptane flames has a non-monotonic behavior, first increasing then slightly decreasing. At 2 bar, the flame has a smaller preheat zone and an appreciable temperature peak in the reaction zone. At 8 bar, this peak flat-

tens out and the temperature profile broadens. This trend extends to 20 bar, where the preheat temperatures are further increased and the profile is flatter and more distributed. This behavior can be predicted using the modified Péclet number, which characterizes the ratio of heat release from the flame to heat removal in a



(a) Image of experimental facility



(b) Schematic of PMB test hardware

Fig. 2. High-pressure test facility SE-5 at NASA GRC: (a) image of experimental facility and (b) schematic of PMB test hardware.

PMB:

$$Pe_{S_l} = \frac{S_l L}{\alpha_g}, \quad (1)$$

where L is the characteristic length scale (e.g., pore diameter), and α_g is the gas thermal diffusivity. The dependence of the laminar flame speed and diffusivity on pressure can be approximated as $P^{-0.5}$ and P^{-1} , respectively. Thus, the ratio of heat release to heat removal increases with increasing pressure ($Pe \propto \sqrt{P}$), which increases the preheat zone temperatures. Furthermore, the heat exchange between the solid and gas phase increases with increasing pressure, as shown in Fig. 1(c), thus leading to enhanced heat recirculation and more distributed temperature profiles.

It is evident that at the same equivalence ratio and mass flux rate, the methane and n-heptane flames differ significantly in structure, preheat length, and exit temperature. In Fig. 1(d)–(f), the free flame temperature profiles are compared to the corresponding PMB case, operated at the laminar flame mass flux, equal to 0.4, 0.87, and 1.34 kg/(m²s), at 2, 8, and 20 bar, respectively, for n-heptane and 0.47 kg/(m²s) at 8 bar for methane. Firstly, the effect of the porous media on the flame temperature profile is illustrated, primarily in increasing the preheat zone and changing the flame structure. Secondly, the predicted steady-state solid temperature profile is shown to closely resemble the gas temperature, except near the flame zone for conditions with low mass-flux rates. In the experimental study, thermocouple measurements, which measure the solid temperature, were used to approximate the flame location. These computational results, as well as previous experiments [24], indicate that using thermocouple measurements of the solid-phase temperature yield sufficient approximations of the flame location.

With an understanding of the high-pressure effects on the flame structure through computational simulations, the high-pressure experimental investigations follow next. The experimen-

tal setup and the results from these measurements are discussed in the next section.

3. Experimental study

3.1. Experimental setup

High-pressure combustion experiments were performed in the SE-5 flame tube facility at the NASA Glenn Research Center (GRC) (see Fig. 2(a) for illustration and Fig. 2(b) for burner schematic). This facility has been used in previous high-pressure combustion studies [25,26]. The internal pressure was maintained by the cooling air flow provided by the central facility compressor (31 bar). The ambient-temperature cooling air was introduced in two locations: at the bottom of the rig for cooling the burner hardware and downstream of the burner to quench-cool the combustion by-products (< 5.0 kg/min). The rig pressure was controlled by a back-pressure valve mounted in the exhaust pipe, which was remotely operated by an auto-feedback process controller to stabilize the desired pressure within 3% deviations. The rig pressure was varied from 2 to 20 bar in the present work, although the burner rig could operate at above 30 bar.

The PMB tested in this study employs a two-zone “interface-stabilized” burner concept comprised of porous foams, which are characterized by pore density measured in pores per inch (ppi). In previous work [11], the PMB design for maximizing flame stability with minimal pressure drop for gaseous methane at atmospheric pressure was experimentally determined. This design consisted of a 3 ppi Silicon Carbide (SiC) downstream section and two 40 ppi Ytria-stabilized Zirconia Alumina (YZA) elements upstream, and is used for the current study as shown in Fig. 3. The SiC foams (Ultramet, Pacoima, CA) were manufactured using chemical vapor deposition (CVD) of SiC, which coats the ligaments of the underlying non-crystalline vitreous carbon foam structure. The YZA

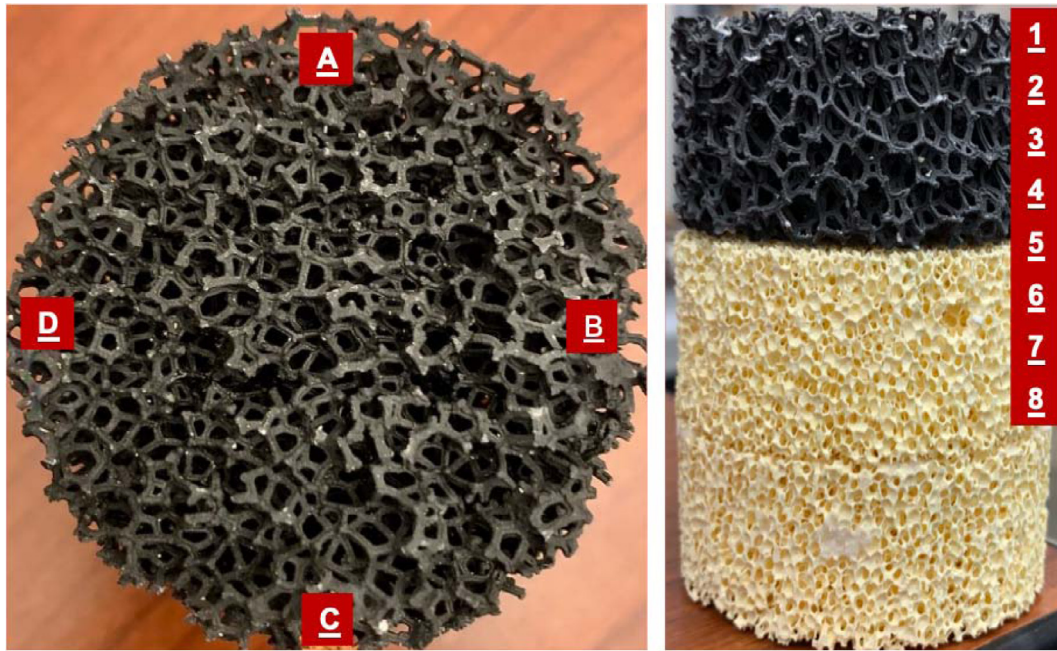


Fig. 3. Azimuthal and axial locations of thermocouples, corresponding to values in Table 1, in SiC (black) element and YZA (yellow) elements. (For interpretation of the references to color in this figure legend, the reader is referred to the web version of this article.)

foams (Selee Corporation, Hendersonville, NC), were made via the sponge replication method and are composed of 62% zirconia, 33% alumina, 2% yttrium and 3% calcium. The three foam components were each 5.08 cm in diameter and 2.54 cm in length and stacked vertically in a castable alumina tube and wrapped in ceramic paper for sealing and insulation.

The PMB assembly with liquid-fuel vaporizer was fit into the vertical-standing, upward-flowing pressure vessel that has an internal diameter of 15 cm with four optical access ports. Note that the optical ports were not used for any observation purpose. Coriolis mass-flow controllers were used to regulate the air and fuel flow rates and thus, controlled the mass flux and global equivalence ratios of the premixed mixture entering the PMB. The mass flow meters for air, CH_4 , and C_7H_{16} (liquid) have 2 to 100% range with maximum readings of 24 kg/h, 1 kg/h, and 1 kg/h, respectively. The flow metering accuracy was 0.5% per reading.

A schematic of the burner and flow system is shown in Fig. 2(b). A nitrogen-pressurized piston-cylinder fuel system delivered liquid n-heptane to the vaporizer, located upstream of the PMB. In the vaporizer, the liquid fuel was drip-fed to a packed column of length 16.5 cm and inner diameter of 1.57 cm filled with stainless-steel spheres (diameter 0.63 cm), which was heated by heat tracing to the desired temperature (~ 500 K) for complete vaporization. Methane fuel was separately (but never simultaneously with the other fuel) fed into the same packed column via a gaseous fuel delivery system with a compressed gas cylinder. Pre-heated (~ 500 K) and pressurized oxidizer air was also routed to the packed column in order to be premixed with the fuel vapor or gaseous fuel (see Fig. 2(b)). Several tests were run to find the adequate length of the packed column to ensure complete vaporization of the fuel. The temperature at the exit of the packed column was monitored to ensure that the fuel/air mixture was formed without condensation or auto-ignition. After the packed column, the mixture flowed through a bend at the base of the system, then upward through a pipe of length of 29.2 cm to the PMB section. The exterior of this pipe was wrapped with electric resistance heat-tape that was controlled (see TE502 in Fig. 2(b)) to provide a constant premixed gas temperature at the inlet to the PMB.

Table 1

Axial locations of the thermocouples, measured from the outlet of the PMB. The thermocouples are positioned at the outer perimeter of the burner at azimuthal locations varying by 90° (see Fig. 3). Note that thermocouple A-3 was damaged in early testing.

Thermocouple	Axial location	Element
A-1, C-1	0 cm	SiC
B-2, D-2	−0.64 cm	SiC
(A-3), C-3	−1.27 cm	SiC
B-4, D-4	−1.93 cm	SiC
A-5, C-5	−2.54 cm	YZA
B-6, D-6	−3.18 cm	YZA
A-7, C-7	−3.81 cm	YZA
B-8, D-8	−4.45 cm	YZA

The PMB section was encased in alumina insulation (3.2 cm thick) and placed inside a stainless steel cylinder (12.7 cm outer diameter). Figure 3 illustrates the setup, with the top-most porous sample referred to as the downstream section and the bottom two samples acting as the upstream flame-arrestor. The temperature was measured using Watlow K-type mineral-insulated thermocouples, with a range of 368–1533 K and standard limits (± 2.2 K). The thermocouples were positioned at the outer perimeter of the burner, placed between the porous media and the ceramic insulation, to monitor the location of the flame at four circumferential quadrants and eight axial locations. The tip of the thermocouple (fully sheathed) was in contact with solid matrix. One of the thermocouples (A-3) was damaged in early testing. The locations of the thermocouples are specified in Table 1, where each thermocouple is identified with a letter corresponding to its azimuthal location and a number corresponding to its axial location (see Fig. 3 for reference), measured from the SiC outlet surface. As found by Zheng et al. [24], a thermocouple inserted inside a porous medium estimates the local solid temperature and the difference between such thermocouple measurements and gas phase temperatures are < 25 K, except near the reaction zone (also illustrated in the computational results in Section 2). As such, measured temperatures were used primarily for observing trends in flame

Table 2

Summary of the test series operating fuel and pressure, as well as the range of tested operating conditions.

Test series	Fuel	Operating pressure (bar)	Mass flux (kg/(m ² s))	Equivalence ratio	Preheat temperature
1	n-Heptane	2	0.71–1.68	0.44–0.61	517–526 K
2	n-Heptane	8	0.86–3.26	0.39–0.55	498–527 K
3	n-Heptane	20	1.37–3.24	0.39–0.49	519–541 K
4	Methane	8	0.68–3.38	0.39–0.55	483–524 K

location. Oxidizer air, fuels, thermocouples and electrical leads for heat tracing were fed through the base flange of the test rig. Instrumentation access ports were located above the PMB section and permitted insertion of a hot surface igniter, static pressure tap, and gas-emissions sampling probe.

The exhaust of the PMB was sampled for emission measurements, then combined with cooling air before flowing into the pressure control valve downstream. As shown in Fig. 2(a) and (b), a nickel-plated stainless-steel sampling probe (12.7 mm outer diameter) was placed in the downstream section of the PMB to extract emissions from the exhaust gas via a single 0.8 mm diameter hole. The probe was designed to work with elevated pressures up to 41 bar and employed pressurized cooling water at flow rates ranging from 0.5 to 3.0 gal/min. The use of water cooling prohibits further reactions of the exhaust products inside the probe. In a preliminary test, five exhaust samples near the walls and centerline over the surface of the PMB were measured, showing only small variations. Thus, the probe design and position in the test rig was assumed to have minimal contribution to the measurement uncertainty of the emission values. The gas pressure of the sample was reduced to slightly above the ambient pressure before it reached a portable gas analyzer (ECOM-EN2F), which measured concentrations of O₂ (0–21 %), CO (0–4000 ppm), NO (0–5000 ppm), and NO₂ (0–1000 ppm), each with $\pm 5\%$ of measurement uncertainty. NO_x was calculated as the sum of NO and NO₂, each having a 5% accuracy of the measurement. NO_x and CO were recorded as part per million by volume (ppm), corrected to 3% O₂ to standardize the effect of air dilution on concentration.

The mixture was ignited 5.4 cm downstream of the porous media. The flame was first stabilized at the outlet of the burner, until the matrix sufficiently heated up to enable the flame to propagate into the porous media. During operation of the embedded flame, emissions and pressure drop properties for a range of mass flux and equivalence ratios were tested. At a given operating condition, the PMB was identified as either stable or unstable, with the latter corresponding to either a blow-off or a flashback condition. The thermocouple measurements and CO emissions were used to track the flame location and stability. At a given equivalence ratio, the boundaries of stability were determined by changing the mass flux by increments of 10%. To establish a new equivalence ratio, the flow conditions were changed by increments of 5% to find the stability boundaries. A stable operating condition was identified when the flame remains inside the SiC element (see Table 1 for axial locations) and all temperature measurements remain constant in time. Blow-off was identified by the formation of CO, and a large decrease in temperature at all four quadrants near the surface (thermocouples A–D at location 1). At certain conditions, a decrease in temperature was observed in only one or two of the four quadrants, without associated CO formation to indicate quenching of the flame. Thus, these conditions were identified as stable. Flashback was identified by a rapid increase in temperature in any thermocouples below the YZA/SiC interface (thermocouples A–D at locations 6–8).

The pressure drop was determined from the measured value of static pressure upstream and downstream of the PMB, using a differential pressure transducer. The upstream tap is shown in

Fig. 2(b) as AP501 in the upstream reactant mixture of the PMB, and the downstream tap is indicated as AP601. The pressure drop of the PMB was measured directly with a differential pressure transducer, PDT501 model 3100D-2-FM-1-1, with range of (0.15–7.5 kPa) and accuracy $\pm 0.75\%$ of full scale. Differences in hydrostatic head and velocity head between the two wall taps were negligible and omitted in the pressure drop result.

Liquid n-heptane was chosen as a neat fuel to alleviate concerns associated with the coking and separation of multi-component fuel into constituents with different vapor pressure, density and heating value. Since gaseous methane fuel was used in the earlier study at atmospheric conditions [11], methane at 8 bar was also tested in this study for performance comparison.

The test series in this study are summarized in Table 2, and the burner performance results for each are discussed in the following section.

3.2. Results and discussion

3.2.1. Flame stability and temperature profiles

For the operating conditions specified in Table 2, the corresponding flame stability and temperature profiles are measured. The regions of burner stability are shown in Fig. 4 for n-heptane and Fig. 5 comparing n-heptane and methane at 8 bar. Solid lines in the stability maps indicate either flashback or blow-off boundaries. All other edges of the stability map are imposed limitations of the mass flow meter and thermocouples. More specifically, vertical boundaries without a solid line are imposed by the limits of the mass flow meters for the air and fuel, and horizontal boundaries (i.e. the upper limit of tested equivalence ratios), are imposed by the measured temperatures in the PMB. To protect the PMB material and the thermocouples, the upper temperature limit for stable operation was set at 1580 K, and thus operating conditions that exceeded this temperature were not tested. In all tests, flashback events occurred more rapidly than liftoff events. Once the flame flashed back in one quadrant, it soon propagated to the other quadrants in the YZA element and eventually to the base of the PMB. In Fig. 4(a) and (b), the size of the symbols represent the CO emissions corresponding to that operating condition, ranging between 0 and 17 ppm. At the lowest stable equivalence ratios and mass flux rates, the flame was stationary but began to quench, as observed by the elevated formation of CO. This limit differs from flashback, where the flame migrated upstream with increased temperature inside the YZA porous media.

With increasing pressure, the flashback boundary and higher mass flux rates moves to leaner conditions, which is predicted by the aforementioned modified Péclet number analysis. Pe_{S_i} , or the ratio of heat release to heat removal, increases with increasing pressure, which increases the preheat temperature thereby increasing the propensity of flashback. The computational results in Section 2 verify this trend, showing that the preheat temperatures increase with pressure (see Fig. 1(b)). A similar increase in flashback propensity was found for methane-fueled PMB operation at pressures up to 11 bar by Noordally et al. [13].

The flame stability maps in Fig. 4(d) and 5(b) have been normalized by the laminar burning flux, $f = \rho_l S_{l,i}$, using local refer-

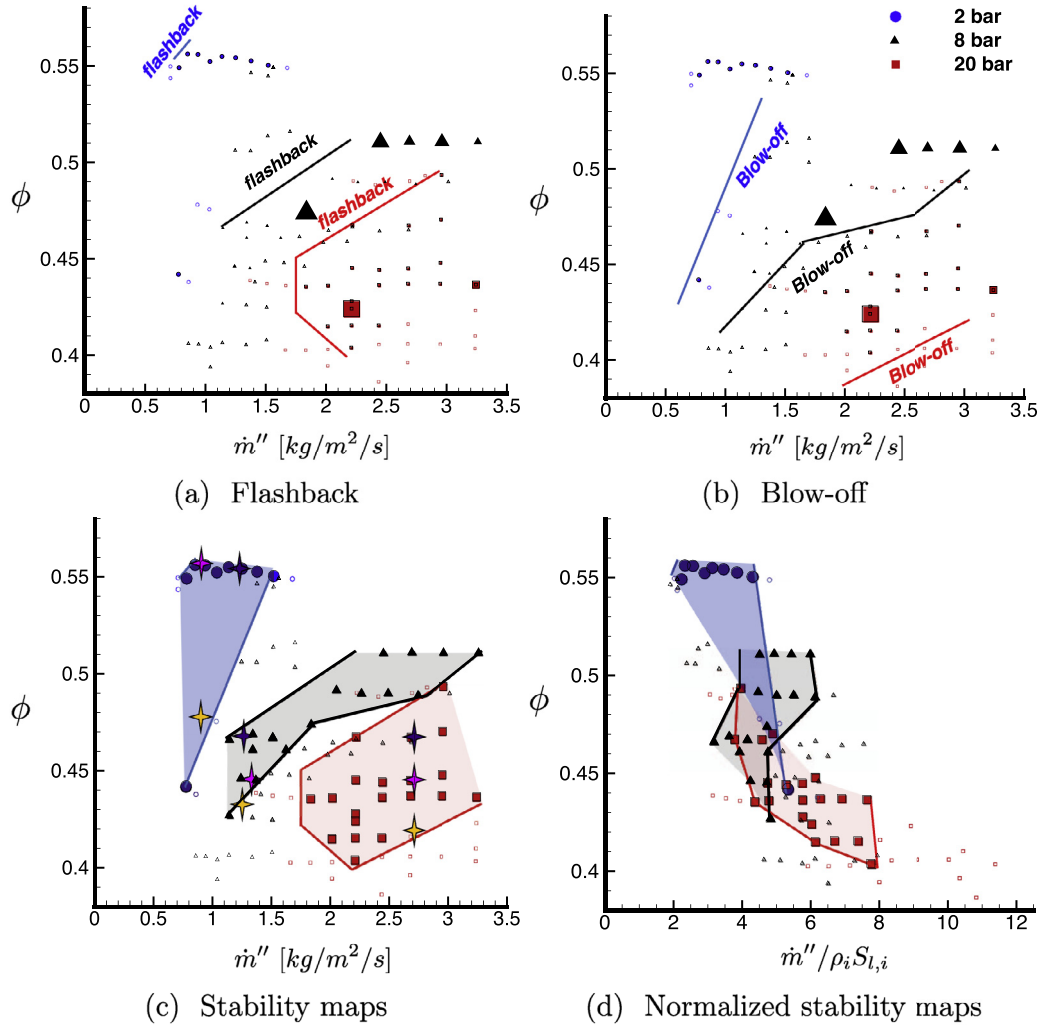


Fig. 4. Stability maps for PMB operation with prevaporized C_7H_{16} : (a), (b) flashback and blow-off boundaries of the stability regimes, with the size of the symbols representing CO emissions between 0 and 17 ppm, (c) compounded flame stability maps, solid lines imply limit of stability, other boundaries determined by limits of the mass flow controllers and thermocouples, (d) compounded stability maps, normalized by the local burning rate. Open symbols denote tested yet unstable conditions.

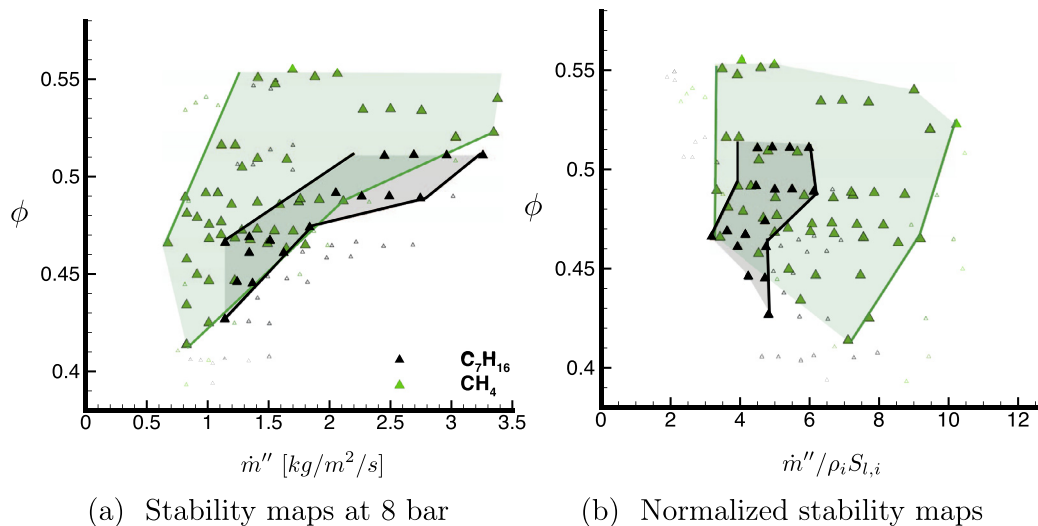


Fig. 5. (a) Comparison of flame stability for C_7H_{16} (black) and CH_4 (green) at 8 bar: (a) stability maps, (b) stability maps normalized by the laminar burning rate. Open symbols denote tested yet unstable conditions. (For interpretation of the references to color in this figure legend, the reader is referred to the web version of this article.)

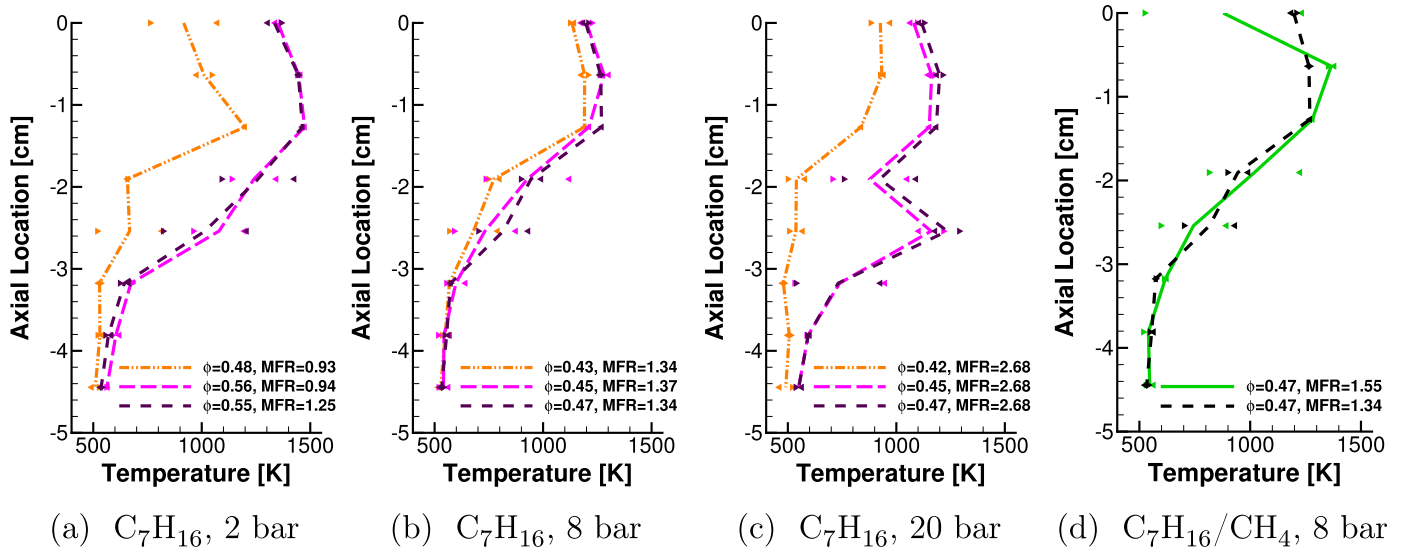


Fig. 6. Temperature profiles at various mass flux rates (MFR) and equivalence ratios, ϕ , of C_7H_{16} flames at (a) 2 bar, (b) 8 bar, and (c) 20 bar marked in Fig. 4(c), where the orange data correspond to near blow-off conditions and the other data correspond to stable operating conditions. (d) Comparison of temperature profiles of C_7H_{16} (black) and CH_4 (green) at 8 bar at similar mass flux rate and $\phi = 0.47$. Symbols \blacktriangleright correspond to thermocouples A and B, and symbols \blacktriangleleft to thermocouples C and D, and the lines correspond to the average temperature at each location. (For interpretation of the references to color in this figure legend, the reader is referred to the web version of this article.)

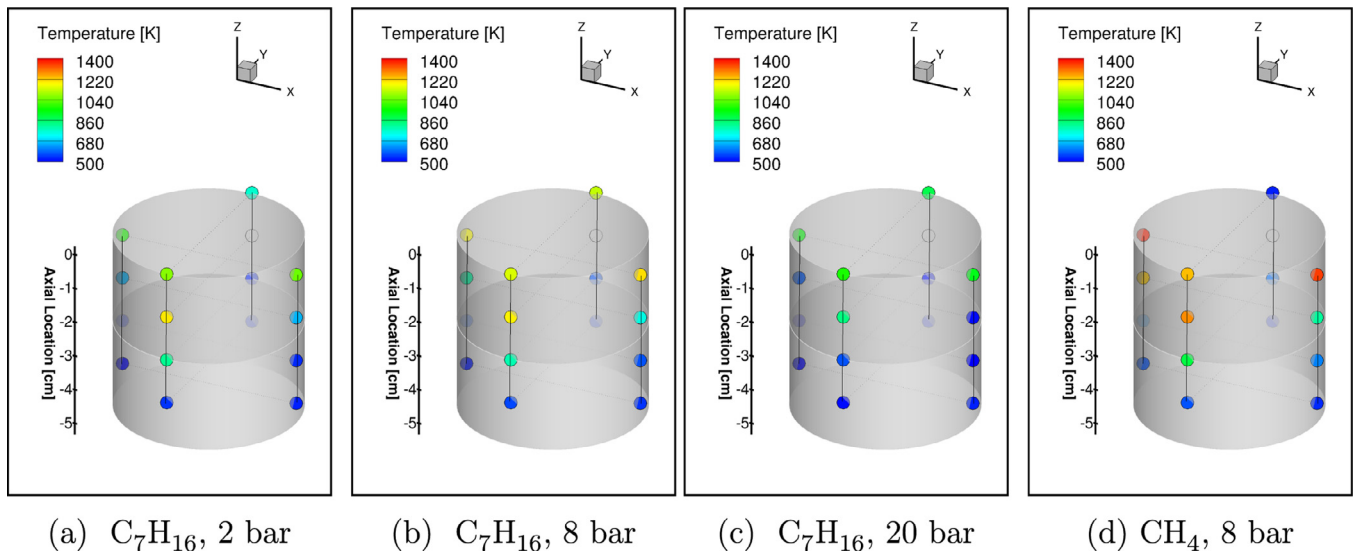


Fig. 7. 3D temperature profile rendering corresponding to the leanest conditions in Fig. 6, (a) $\phi = 0.48$, $0.93 \text{ kg}/(\text{m}^2\text{s})$, (b) $\phi = 0.43$, $1.34 \text{ kg}/(\text{m}^2\text{s})$, (c) $\phi = 0.42$, $2.68 \text{ kg}/(\text{m}^2\text{s})$, (d) $\phi = 0.47$, $1.55 \text{ kg}/(\text{m}^2\text{s})$.

ence quantities as a function of burner inlet temperature, pressure, and equivalence ratio. The effect of the porous media on the combustion performance and flame stabilization is highlighted by this normalization. Figures 4(d) and 5(b) show an increase in the normalized mass flux by up to six to ten times for n-heptane and methane, respectively. After normalization, the results showed a significantly higher blow-off boundary in the stability regime for methane than n-heptane, as indicated by the solid lines in Fig. 5(b).

Temperature profiles of n-heptane flames at 2 bar, 8 bar, and 20 bar marked in Fig. 4(c) are shown in Fig. 6. Thermocouple temperature measurements at each axial location illustrate significant tilting of the flame for certain conditions. Increasing equivalence ratio results in increasing peak temperature. Furthermore, similar to the computational temperature profiles shown in Section 2, the experimental temperature profiles become more flattened as the pressure increases, exhibiting higher preheat temperatures.

Figure 6 (d) compares the flame profiles of comparable stable operating conditions for n-heptane and methane at 8 bar. Although a similar average temperature profile was measured, the methane flame is significantly more inhomogeneous in the azimuthal direction and lift-off at thermocouple A-1 is observed. The flame heterogeneities and tilting are further illustrated in Fig. 7 for the leanest conditions shown in Fig. 6. Flame tilting was also observed in a previous study of gaseous methane at atmospheric pressure, with the same PMB matrix composition [11]. The study by Hsu et al. [27] attributed the flame tilting to the formation of fissures that disturb the otherwise uniform flow distribution as well as the local thermophysical properties of the solid matrix. Such fissures were indeed observed in the porous matrix post-combustion in X-ray Computed Tomography scans (see Section 4). Furthermore, computational studies of filtration gas combustion identify flame inclination as one of two key flame-front

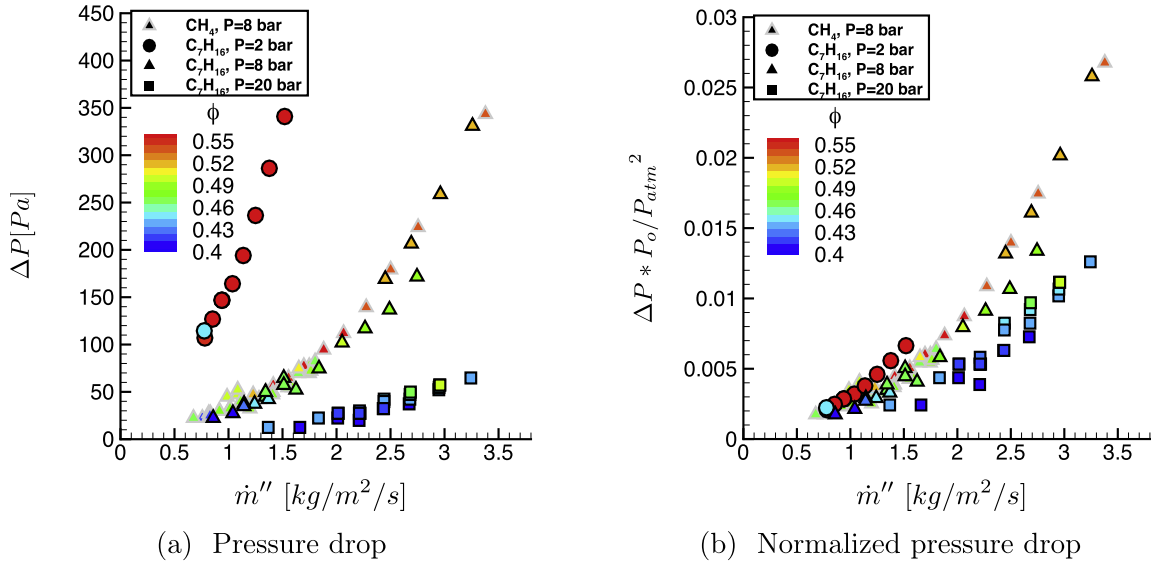


Fig. 8. Measurements of pressure drop at stable operating conditions, where symbols correspond to operating pressure at 2 bar (•), 8 bar (▲) and 20 bar (■).

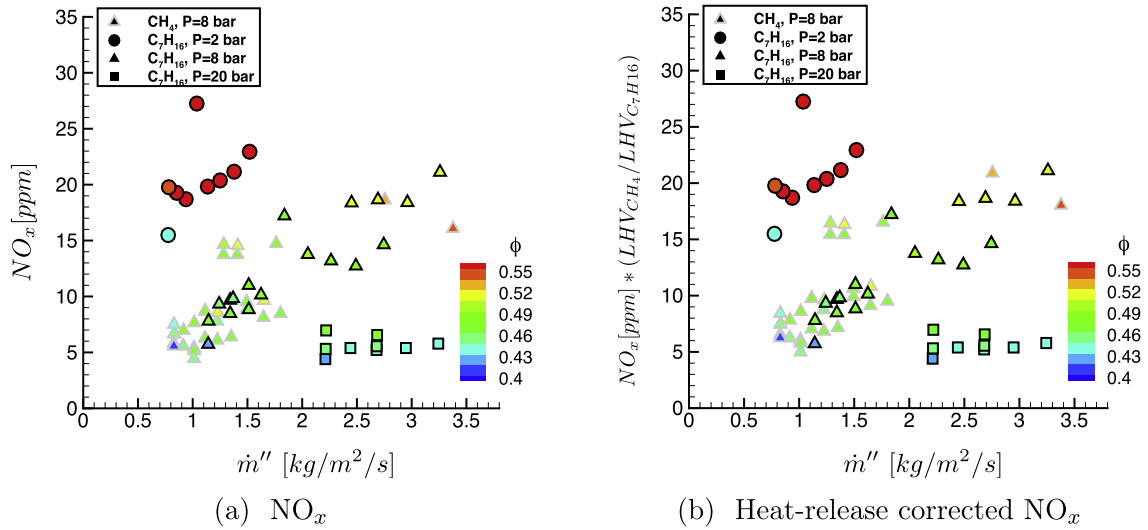


Fig. 9. Emission measurements at stable operating conditions for both methane and n-heptane fuels, at 2 bar (•), 8 bar (▲) and 20 bar (■).

instabilities in flame propagation in packed-bed porous media [28–30].

3.2.2. Pressure drop

The pressure drop for both n-heptane and methane flames increases with increasing mass flux rate. According to the Darcy–Forchheimer model:

$$d_x P = -\frac{\mu}{K_1} u - \frac{\rho}{K_2} u^2, \quad (2)$$

where u is the Darcy velocity, ρ is the density, K_1 is the intrinsic permeability and K_2 is the non-Darcian drag coefficient, estimated using Ergun's equation [31].

To isolate the effect of the operating pressure, the total pressure drop across the porous matrix can be expressed by integrating Eq. (2) along the axial direction and substituting the ideal gas law to relate pressure and density:

$$\Delta P = -\int_0^x \frac{RT}{P_o} \left[\frac{\mu}{K_1} \frac{\dot{m}''}{\epsilon} + \frac{1}{K_2} \left(\frac{\dot{m}''}{\epsilon} \right)^2 \right] dx. \quad (3)$$

Thus, for an equivalent temperature profile, the pressure drop is estimated to be lower at higher operating pressures. This is confirmed by the measured pressure drop shown in Fig. 8(a). By multiplying the measured pressure drop by the operating pressure, the results begin to collapse as shown in Fig. 8(b). The results for higher pressures still remain slightly lower, due to the lower peak temperatures at these conditions.

3.2.3. Emissions

Emissions of NO_x and CO, corrected to 3 % O_2 , are shown in Fig. 9 for both fuels at elevated pressures and stable operating conditions. Since all temperatures are below 1800 K, thermal NO production is insignificant, and the prompt NO pathway is dominant [32]. The NO_x emissions decrease at higher pressures, since the stability regime shifted to leaner conditions with increasing pressure. For stable operating conditions, NO_x emissions increase with increasing mass flux rate and equivalence ratio due to higher local temperatures in the burner, as indicated by thermocouple measurements. Near the minimum stability limit (i.e. lower equivalence ratio and mass flux), the CO emissions are increased for both fuels since the flame is starting to quench. Similarly, near the blow-

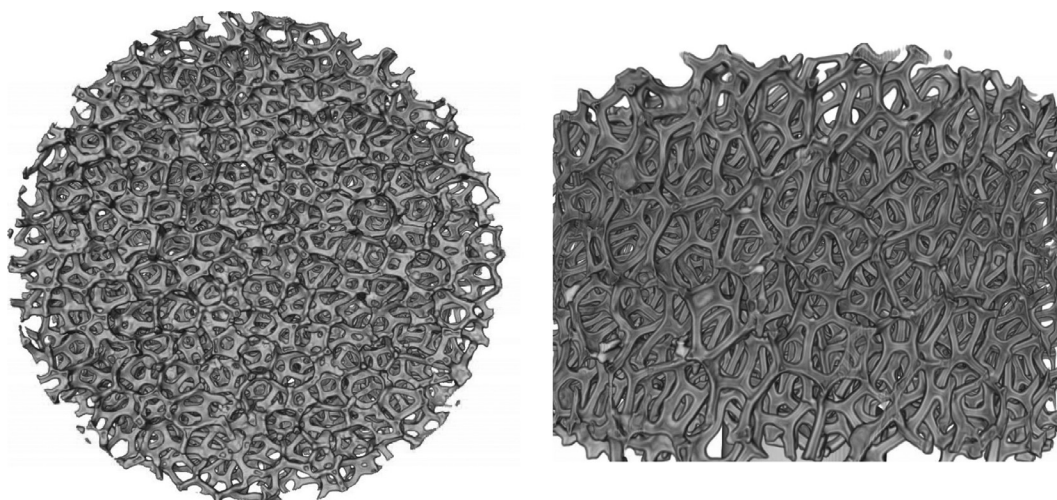


Fig. 10. Top and side view of the XCT isosurface of the full SiC porous foam matrix (5.08 cm diameter and 2.54 cm height) in the downstream zone of the burner, post-combustion, after a total of 2 h of operation. Scan acquisition parameters correspond to Scan 1 in Table 3.

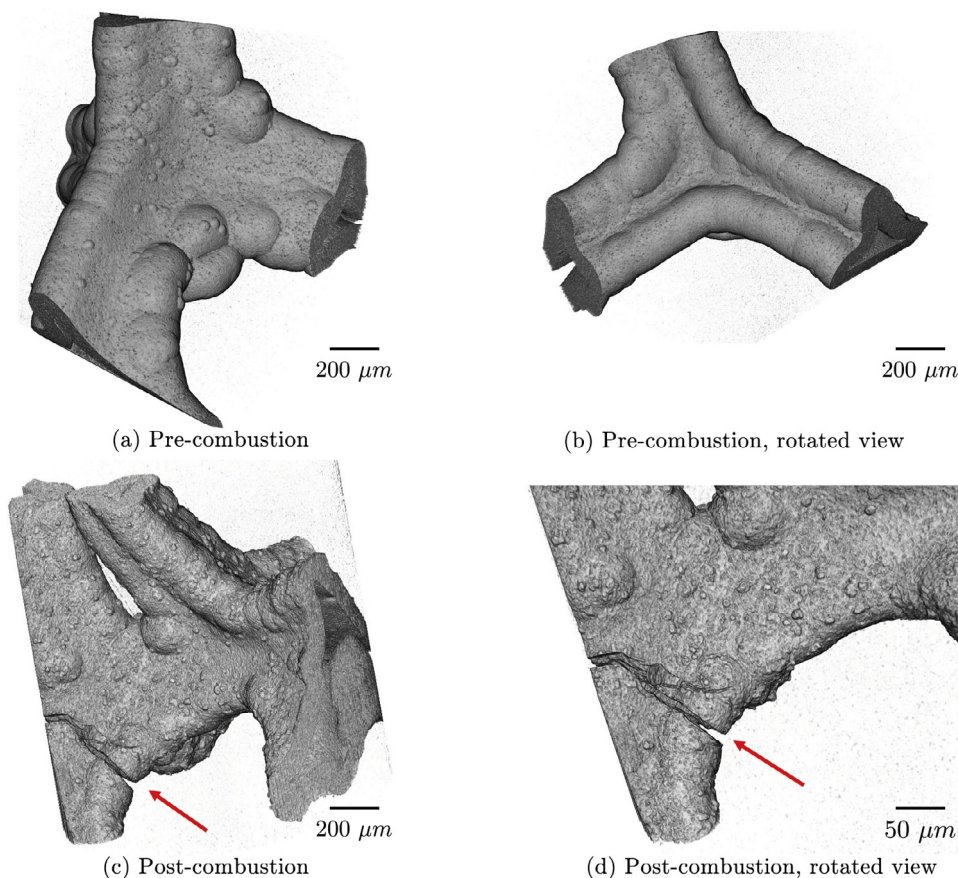


Fig. 11. XCT isosurface of a strut in 1.8 mm field of view of the SiC porous foam matrix in the downstream zone of the burner, pre- and post-combustion, where the arrow indicates the location of the crack. XCT-acquisition parameters correspond to Scan 2 in Table 3.

off and flashback boundaries, the local temperature begins to decrease and incomplete combustion results in higher CO emissions. Kaplan and Hall [15] performed experimental tests at atmospheric pressure where the liquid n-heptane fuel was sprayed directly onto a porous foam upstream of the main PMB, and reported similar CO and NO_x emissions as those of the current study at 2 bar (i.e., 3–7 ppm CO and 15–20 ppm NO_x). For all stable operating conditions, NO_x measurements were below 25 ppm and mostly complete CO combustion was observed, with a maximum of 17 ppm.

4. X-ray computed tomography analysis

The PMB experiments were performed over four days, during which the burner underwent dozens of on-and-off cycles and a total of over 22 hours of operation. To examine the structural integrity of the porous matrix over the course of the combustion tests, the 3 ppi SiC sample was analyzed using a ZEISS XRADIA 520 VERSA X-ray Microscope (XRM) for X-ray Computed Tomography (XCT). As the resolution capability of the XRM decreases with

Table 3
Acquisition parameters of the XCT scans.

Scan	Resolution	Field of view	Voltage	Current
1	1.8 μm	1.8 mm	110 kVp	91 mA
2	89.6 μm	Full domain	60 kVp	83 mA

increasing field-of-view, the whole domain was first scanned at a resolution of 89.8 μm to identify large-scale structural defects. Subsequently, a high-resolution scan of a strut was performed to identify small-scale cracks and surface properties. The acquisition parameters of the two scans, performed with projections over 360°, are summarized in Table 3.

Automatic 3D segmentation and isosurface rendering was performed using the Avizo software to visualize the structure, as shown in Figs. 10 and 11. The pre- and post-combustion scans of the full domain were nearly identical, and showed no apparent signs of large-scale degradation. The isosurface of the matrix post-combustion is shown in Fig. 10. However, the higher resolution scan revealed fissures ($\sim 20 \mu\text{m}$ wide) in the struts of the matrix structure. Thus, high-resolution methods are required to fully examine the material degradation of the ceramic matrix foams. However, the matrix proved to be durable in withstanding the over 22 h of operation, thermal stresses due to on-and-off cycling, and high pressure conditions. In addition to the fissures, the high-resolution scans reveal an increase in the solid surface roughness after combustion. SiC oxidizes at high temperatures, leading to oxide bubble formation and solid SiO_2 deposition on the matrix structure [33–35]. Aronovici et al. [35] found that the formation of an oxide layer on SiC lattice drastically reduces the effective thermal conductivity, while changes in pressure drop are insignificant. Although the XCT scans indicate the potential of oxide layer deposition after high pressure PMB operation, further analysis of the material composition is needed to identify the cause of the apparent surface transformation and its effects on the burner performance.

5. Conclusions

In this work, the performance of a Porous Media Burner (PMB) that was operated with pre-vaporized liquid fuel at high-pressure conditions was examined. Combustion stability regimes, temperature, pressure drop, CO and NO_x emissions were measured and X-ray Computed Tomography (XCT) analysis was performed to examine the structural integrity of the porous matrix during high-pressure combustion. Experiments were conducted in NASA's high-pressure facility SE-5 at 2, 8, and 20 bar absolute pressure using n-heptane fuel with preheat temperatures of around 500 K. For performance comparisons, the burner was also tested with methane at 8 bar. After normalization with the laminar burning rate, the results showed a significantly larger stability regime for methane than n-heptane. For all tests, the burning velocity in the PMB was measured up to ten times higher than the laminar flame speed. Trends in flame flashback were found to be well predicted by the modified Péclet number, illustrating a higher mass flux flashback boundary with increasing pressure. These experimental investigations were complemented by numerical simulations to examine effects of the pressure and liquid fuel on the flame structure. These simulations confirmed the increase in preheat-zone temperatures and propensity for flashback with increasing pressure. The pressure drop was shown to decrease with increasing pressure, although independent of fuel. NO_x measurements were below 25 ppm for all stable operating conditions, for which complete oxidation of CO was observed. At 20 bar conditions, stable operation at very low values of equivalence ratio were found, with corresponding values of NO_x below 5 ppm.

Additionally, this work demonstrated the utility of applying lab-scale XCT diagnostics for investigating the material and structural processes in porous foams. The XCT analysis revealed small-scale fissures, but no large-scale defects were observed in the SiC porous matrix after extensive high-pressure testing. In future work, this tool can be combined with Energy Dispersive X-ray Analysis to study the surface properties and compositions of ceramic materials used in PMBs, and to help develop durable porous foams for long-term operation at elevated pressures.

Although PMBs have been previously identified as an advanced combustion technology capable of reducing emissions and increasing system efficiency, most of the existing literature on PMBs are limited to gaseous fuels operated at atmospheric pressure conditions. The current study extends to pre-vaporized liquid fuels and elevated pressures to demonstrate the viability of porous media combustion for application to gas-turbine engines and presents quantitative trends at engine-relevant conditions. Future studies are needed to test the performance with transportation fuels as well as the effects of liquid-fuel evaporation.

Declaration of Competing Interest

The authors declare that they have no known competing financial interests or personal relationships that could have appeared to influence the work reported in this paper.

Acknowledgments

This work was supported by a Leading Edge Aeronautics Research for NASA (LEARN) grant (Award no. NNX15AE42A) and by the National Science Foundation through a Graduate Research Fellowship (No. 1656518) and Award CBET-1800906. Part of this work was performed at the Stanford Nano Shared Facilities (SNSF), supported by the National Science Foundation under award ECCS-1542152.

References

- [1] S. Wood, A.T. Harris, Porous burners for lean-burn applications, *Progr. Energy Combust. Sci.* 34 (5) (2008) 667–684.
- [2] M.A. Mujeebu, M.Z. Abdullah, M.Z.A. Bakar, A.A. Mohamad, R.M.N. Muhad, M.K. Abdullah, Combustion in porous media and its applications – a comprehensive survey, *J. Environ. Manag.* 90 (8) (2009) 2287–2312.
- [3] S. Sobhani, D. Mohaddes, E. Boigne, P. Muhunthan, M. Ihme, Modulation of heat transfer for extended flame stabilization in porous media burners via topology gradation, *Proc. Combust. Inst.* 37 (4) (2019) 5697–5704.
- [4] D. Trimis, F. Durst, Combustion in a porous medium – advances and applications, *Combust. Sci. Technol.* 121 (1–6) (1996) 153–168.
- [5] V.S. Babkin, A.A. Korzhavin, V.A. Bunev, Propagation of premixed gaseous explosion flames in porous media, *Combust. Flame* 87 (1991) 182–190.
- [6] Y. Kotani, T. Takeno, An experimental study on stability and combustion characteristics of an excess enthalpy flame, *Symposium (International) on Combustion* 19 (1982) 1503–1509.
- [7] J.R. Howell, M.J. Hall, J.L. Ellzey, Combustion of hydrocarbon fuels within porous inert media, *Progr. Energy Combust. Sci.* 22 (2) (1996) 121–145.
- [8] A.J. Barra, J.L. Ellzey, Heat recirculation and heat transfer in porous burners, *Combust. Flame* 137 (1–2) (2004) 230–241.
- [9] M.K. El-Hossaini, M. Maerefat, K. Mazaheri, Numerical investigation on the effects of pressure drop on thermal behavior of porous burners, *J. Heat Transf.* 130 (3) (2008) 032601.
- [10] I. Malico, J.F. Pereira, Numerical study on the influence of radiative properties in porous media combustion, *J. Heat Transf.* 123 (5) (2001) 951–957.
- [11] S. Sobhani, B. Haley, D. Bartz, J. Dunnmon, J. Sullivan, M. Ihme, Investigation of lean combustion stability, pressure drop, and material durability in porous media burners, *Proceedings of the ASME Turbo Expo 2017: Turbomachinery Technical Conference and Exposition*, Volume 5C: Heat Transfer, Turbo Expo: Power for Land, Sea, and Air, American Society of Mechanical Engineers Digital Collection (2017). V05CT17A001
- [12] C. Bedoya, I. Dinkov, P. Habisreuther, N. Zarzalis, H. Bockhorn, P. Parthasarathy, Experimental study, 1D volume-averaged calculations and 3D direct pore level simulations of the flame stabilization in porous inert media at elevated pressure, *Combust. Flame* 162 (10) (2015) 3740–3754.
- [13] E. Noordally, J.M. Przybylski, J.J. Witton, Porous Media Combustors for Clean Gas Turbine Engines, Technical Report, DTIC Document, 2004.

- [14] A. Bakry, A. Al-Salaymeh, A.H. Al-Muhtaseb, A. Abu-Jrai, D. Trimis, Adiabatic premixed combustion in a gaseous fuel porous inert media under high pressure and temperature: novel flame stabilization technique, *Fuel* 90 (2) (2011) 647–658.
- [15] M. Kaplan, M.J. Hall, The combustion of liquid fuels within a porous media radiant burner, *Exp. Therm. Fluid Sci.* 11 (1) (1995) 13–20.
- [16] C.-J. Tseng, J.R. Howell, Combustion of liquid fuels in a porous radiant burner, *Combust. Sci. Technol.* 112 (1) (1996) 141–161.
- [17] S. Vijaykant, A.K. Agrawal, Liquid fuel combustion within silicon-carbide coated carbon foam, *Exp. Therm. Fluid Sci.* 32 (1) (2007) 117–125.
- [18] H. Takami, T. Suzuki, Y. Itaya, M. Hasatani, Performance of flammability of kerosene and NO_x emission in the porous burner, *Fuel* 77 (3) (1998) 165–171.
- [19] S. Jugjai, N. Wongpanit, T. Laoketkan, S. Nokkaew, The combustion of liquid fuels using a porous medium, *Exp. Therm. Fluid Sci.* 26 (1) (2002) 15–23.
- [20] D. Mohaddes, M. Ihme, C.T. Chang, Superadiabatic matrix-stabilized combustion for gas turbine engine performance improvement, *Under Rev.* (2019).
- [21] M. Kaviany, *Principles of Heat Transfer in Porous Media*, Springer Science & Business Media, 1991.
- [22] T. Lu, C.K. Law, C.S. Yoo, J.H. Chen, Dynamic stiffness removal for direct numerical simulations, *Combust. Flame* 156 (8) (2009) 1542–1551.
- [23] A. Kazakov, M. Frenklach, Reduced reaction sets based on GRI-Mech 1.2. Available from <http://www.me.berkeley.edu/drm>.
- [24] C. Zheng, L. Cheng, A. Saveliev, Z. Luo, K. Cen, Gas and solid phase temperature measurements of porous media combustion, *Proc. Combust. Inst.* 33 (2) (2011) 3301–3308.
- [25] J.J. Kojima, D.G. Fischer, Multiscalar analyses of high-pressure swirl-stabilized combustion via single-shot dual-SBG Raman spectroscopy, *Combust. Sci. Technol.* 185 (12) (2013) 1735–1761.
- [26] J.J. Kojima, D.G. Fischer, J.-Y. Chen, Code-validation scalar measurements in high-pressure hydrogen-added methane combustion, *J. Propul. Power* (2016) 285–304.
- [27] P.-F. Hsu, W.D. Evans, J.R. Howell, Experimental and numerical study of premixed combustion within nonhomogeneous porous ceramics, *Combust. Sci. Technol.* 90 (1–4) (1993) 149–172.
- [28] S.S. Minaev, S.I. Potytnyakov, V.S. Babkin, Combustion wave instability in the filtration combustion of gases, *Combust. Explos. Shock Waves* 30 (3) (1994) 306–310.
- [29] K. Dobrego, S. Zhdanok, A. Zaruba, Experimental and analytical investigation of the gas filtration combustion inclination instability, *Int. J. Heat Mass Transf.* 44 (11) (2001) 2127–2136.
- [30] J. Zhang, L. Cheng, C. Zheng, Z. Luo, M. Ni, Numerical studies on the inclined flame front break of filtration combustion in porous media, *Energy and Fuels* 27 (8) (2013) 4969–4976.
- [31] S. Ergun, A.A. Orning, Fluid flow through randomly packed columns and fluidized beds, *Indust. Eng. Chem.* 41 (6) (1949) 1179–1184.
- [32] J.A. Miller, C.T. Bowman, Mechanism and modeling of nitrogen chemistry in combustion, *Progr. Energy Combust. Sci.* 15 (4) (1989) 287–338.
- [33] N.S. Jacobson, Corrosion of silicon-based ceramics in combustion environments, *J. Am. Ceram. Soc.* 76 (1) (1993) 3–28.
- [34] S. Gianella, D. Gaia, A. Ortona, High temperature applications of Si–SiC cellular ceramics, *Adv. Eng. Mater.* 14 (12) (2012) 1074–1081.
- [35] M. Aronovici, G. Bianchi, L. Ferrari, M. Barbato, S. Gianella, A. Ortona, Heat and mass transfer in ceramic lattices during high-temperature oxidation, *J. Am. Ceram. Soc.* 98 (8) (2015) 2625–2633.